Nano Research

Open Access

Research Article

Multiphase structures build heterogeneous interfaces to promote interface polarization loss electromagnetic waves

Zhiqiang Guo[1,2,§], Yuhang Cheng[1,§], Di Lan[1] ✉, Siyuan Zhang[3], Zirui Jia[2,4] ✉, and Guanglei Wu[2] ✉

[1] *School of Automotive Materials, Hubei University of Automotive Technology, Shiyan 442002, China*
[2] *College of Materials Science and Engineering, Qingdao University, Qingdao 266071, China*
[3] *School of Chemistry and Chemical Engineering, Northwestern Polytechnical University, Xi'an 710072, China*
[4] *College of Chemistry and Chemical Engineering, Qingdao University, Qingdao 266071, China*
[§] *Zhiqiang Guo and Yuhang Cheng contributed equally to this work.*

Cite this article: *Nano Research*, **2025**, *18*, 94907808. https://doi.org/10.26599/NR.2025.94907808

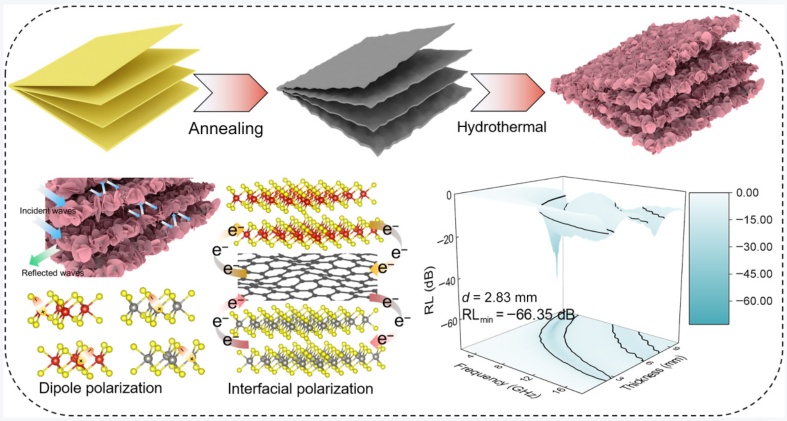

ABSTRACT: In view of the current serious electromagnetic pollution problem, it is urgent to study efficient electromagnetic wave absorbing materials. The construction of multiphase inhomogeneous interfaces is an effective means, especially for the fine design of multicomponent materials. In this study, multiphase composites with tunable heterogeneous interfaces were prepared by hydrothermal synthesis, carbon coating and high-temperature annealing processes. Multiple component composites constructed rich heterogeneous interfaces, which exhibited strong interfacial polarization effects and effectively improved the absorption efficiency of electromagnetic wave (EMW). The fine tuning of the heterogeneous interfaces is achieved through component adjustment, which enhances the charge carrier transport efficiency and the polarization loss capability. Ultimately, the multiphase VS_2@C@WS_2 composites obtained excellent EMW absorption performance, with the minimum reflection loss and the maximum effective absorption bandwidth of −66.35 dB and 5.12 GHz, respectively. In this work, the controllable construction of heterogeneous interfaces is achieved through the tuning of components, which provides a valuable method for optimizing the polarization loss.

KEYWORDS: multiphase structure, heterogeneous interfaces, polarization loss, electromagnetic wave absorption

1 Introduction

The rapid development of modern science and technology has brought convenience to human production and life, but also caused electromagnetic pollution. The development of efficient electromagnetic wave (EMW) absorbing materials is an effective strategy to solve this problem [1–3]. Multiphase heterogeneous interfacial composites are ideal for the preparation of efficient EMW absorbing materials. However, the controllable construction of interfaces with multiphase structures remains an important challenge at present [4].

Multiphase structural materials composed of multiple different phases have differences in composition, crystal structure and other aspects among each phase [5]. It can be synthesized through physical mixing, chemical synthesis and other methods, and by means of multiphase combination, multiple properties that a single material cannot possess can be obtained. In multiphase structured materials, non-homogeneous interfaces are formed in the junction region due to the presence of multiphases with different physicochemical properties. The charge at the heterogeneous interface is redistributed to form a localized electric field, which significantly improves the carrier migration efficiency and enhances the EMW absorption [6, 7]. The construction of multiphase heterogeneous interfaces is an effective way to enhance the

Received: June 15, 2025; **Revised:** July 8, 2025
Accepted: July 15, 2025

✉Address correspondence to Di Lan, landi@mail.nwpu.edu.cn; Zirui Jia, jiazirui@qdu.edu.cn; Guanglei Wu, wuguanglei@mail.xjtu.edu.cn, wuguanglei@qdu.edu.cn

dielectric polarization response to broaden the absorption performance of EMW. Chen et al. [8] prepared FeS/MoS_2@N doped carbon sandwich wall nanotubes (FeMoS-SWCNT) using a ligand exchange strategy of sulfurization process. FeMoS-SWCNT obtained excellent EMW absorption performance due to the interfacial polarization caused by the electronic interaction of multiple interfaces (FeS/N doped carbon (NC), MoS_2/NC and FeS/MoS_2). Wu et al. [9] constructed multiple groups of Cu–S–O through a solvent engineering heterogeneous process with fine control. The CuS/CuO/S heterogeneous interface and sulfur vacancies were constructed, which effectively enhanced the polarization loss and achieved an excellent absorption intensity of −43.05 dB with a broadband response of 7.54 GHz. However, there are few studies on the controllable construction of transition metal sulfide heterogeneous interfaces, and the explanation is not in-depth enough [10–12]. However, the controlled construction of heterogeneous interfaces in multiphase structures has been less studied and not well explained. Therefore, the development of efficient EMW absorbing materials with multiphase structures is a difficult task.

Transition metal sulfides have rich chemical compositions, diverse crystal structures and unique physicochemical properties. Among them, VS_2 and WS_2 have tunable dielectric properties and excellent impedance matching capability. Their high dielectric constants and controlled conductivity effectively reduce surface reflections and enhance the ability of electromagnetic waves to enter the interior of the material [13, 14]. Their two-dimensional (2D) layered structure confers lightweight, flexibility and structural design flexibility. Polarization relaxation loss can be effectively promoted by nanostructure design and impedance matching optimization. Piao et al. [15] prepared a binary flower-like WS_2/Co hybrid composite anchored with WS_2, which effectively improved dielectric loss and achieved excellent EMW absorption performance. Cao et al. [16] modified the surface of VS_2 with biomass glucose-derived carbon (GDC) by hydrothermal method and then carbonized it at high temperature. A VS_2/GDC hybrid material with a multi-interface heterogeneous structure was realized, which enhanced the EMW absorption performance. Multiphase heterostructures were constructed by combining VS_2 or WS_2 with other materials to optimize the interfacial polarization loss EMW.

In this work, multicomponent transition metal sulfide composites containing heterogeneous structures were prepared by hydrothermal synthesis, high-temperature annealing and carbon coating processes. Firstly, prepared flakes of VS_2 provided the basic carrier structure, and the interfacial bonding ability between the materials was improved by the carbon capping process. Finally, WS_2 nanosheets were grown on the surface of VS_2@C to form a composite with a multiphase heterogeneous interface (VS_2@C@WS_2). The differences in material properties of VS_2, C, and WS_2 directly due to the differences in material properties prompted the migration of charge carriers at the interface to produce an interfacial polarization effect and enhance the EMW loss capability. After the effect of enhanced interfacial polarization, the VS_2@C@WS_2 composite obtained an RL of −66.35 and an EAB of 5.12 GHz at 2.83 and 2.4 mm, respectively. This study provides new insights into the construction of multiphase structural composites and contributes to the development of efficient EMW absorbing materials.

2 Experimental section

2.1 Materials

Ammonia ($NH_3 \cdot H_2O$), ammonium metavanadate (NH_4VO_3), thioacetamide (TAA), trimethylolaminomethane (Tris), dopamine hydrochloride, tungsten dichloride (WCl_2), and N,N-dimethylformamide (DMF) were purchased from Shanghai Maclean Biochemical Technology Co., LTD. All reagents were used directly without further purification..

2.2 Synthesis of VS_2

0.7 g of NH_4VO_3 and 2.4 g of TAA were added to 9 mL of $NH_3 \cdot H_2O$ and 45 mL of deionized water and stirred thoroughly. Subsequently, VS_2 was obtained by holding at 160 °C for 20 h.

2.3 Synthesis of VS_2@C

An amount of VS_2 prepared above was added to 100 mL of deionized water with 0.231 g of Tris and 0.1 g of dopamine hydrochloride and stirred overnight. Subsequently, VS_2@C was obtained by holding at 400 °C for 3 h in an argon atmosphere.

2.4 Synthesis of VS_2@C@WS_2

0.02 g of VS_2@C prepared above was added to 60 mL DMF solution with 0.198 g of WCl_2 and 0.375 g of TAA and stirred well. Subsequently, VS_2@C@WS_2 was obtained by holding at 200 °C for 12 h.

2.5 Characterization

The crystal structures of all samples were characterized using X-ray diffraction (XRD) (λ = 0.15418 nm). Raman spectra were recorded at 532 nm using a Renishaw InviaPlus micro-Raman spectroscopy system equipped with a 50 mW diode-pumped solid-state (DPSS) laser. The microstructure, morphology, and element distribution of the samples were observed using a field emission scanning electron microscope (SEM, JEOLJSM7800F) equipped with energy dispersive spectrometer (EDS), as well as a transmission electron microscope (TEM, JEOLJEM2100). The elemental composition and chemical bond state of the samples were determined via X-ray photoelectron spectroscopy (XPS).

A vector network analyzer (N5234A, Agilent) was accustomed to characterize the electromagnetic parameters at 2–18 GHz and further analyzed the Electromagnetic wave absorption (EWA) characteristics of the samples. Prior to testing, the prepared samples were uniformly dispersed in the paraffin matrix with a filling amount of 5 wt.%. Then, the mixture was pressed into a ring shape (φ_{out}: 7.00 mm, φ_{in}: 3.04 mm, thickness: 2.0 mm). In general, the electromagnetic absorption characteristics of EWA materials are related to complex permittivity and complex permeability. The reflection loss can be calculated according to the transmission line theory [17–19]

$$\mathrm{RL\,(dB)} = 20\lg\left|\frac{Z_{in} - Z_0}{Z_{in} + Z_0}\right| \tag{1}$$

$$Z_{in} = Z_0\sqrt{\frac{\mu_r}{\varepsilon_r}}\tanh\left(j\frac{2\pi fd}{c}\sqrt{\mu_r\varepsilon_r}\right) \tag{2}$$

where Z_{in} and Z_0 represent the input impedance and free space impedance of the normalized absorber, respectively, while ε_r and μ_r represent the complex permittivity and complex permeability, f is the frequency of the electromagnetic wave, c is the propagation speed of light in free space, and d is the thickness of the absorber.

3 Result and discussion

In Fig. 1(a), the synthesis process of multicomponent VS_2@C@WS_2 composites with multiphase heterogeneous interfaces is shown. First, ammonium metavanadate dissociates vanadate ions (VO^{3-}) and ammonium ions (NH^{4+}) under alkaline conditions, and thioacetamide releases sulfur ions (S^{2-}). Then, at high temperature, VO^{3-} is reduced to V^{4+}, which reacts with S^{2-} to form VS_2. VS_2 is used as the substrate, which is coated with PDA and annealed at high temperature to form a graphitic carbon layer. After carbon coating, it can enhance the surface activity of the material, increase the interfacial compatibility, and help the adhesion of other materials. Finally, WCl_2 and TAA react at high temperatures to produce nanosheet-like structures WS_2 anchored to the material surface. In the XRD images, the positions at 15.4°, 35.7°, and 45.2° correspond to the (001), (101), and (102) crystal planes of VS_2 (PDF #36-1139), respectively (Fig. 1(b)). After carbon coating, a distinct carbon peak appeared in the range of 20°–30°, while the diffraction peak of VS_2 was perfectly retained, demonstrating the synthesis of VS_2@C material (Fig. 1(c)). The VS_2@C was further modified by growing WS_2 nanosheets on the surface, and the diffraction peaks located at 9° and 18° corresponded to the (002) and (004) crystal faces of 1T-WS_2 (Fig. 1(d)) [20–22]. The diffraction peaks corresponding to the (002) crystal face of 1T-WS_2 were somewhat shifted (PDF #08-0237) due to the NH^{4+} intercalation (PDF #08-0237) released by the excess thioacetamide [23]. After modification by WS_2, the diffraction peaks of VS_2 and C were still clearly visible, demonstrating the successful synthesis of multicomponent VS_2@C@WS_2 materials with multiphase heterogeneous interfaces. The crystal structures of VS_2 and WS_2 are shown in Fig. 1(e).

The degree of graphitization and defects in the material were analyzed using Raman tests, and two distinct diffraction peaks at 1351 and 1590 cm^{-1} indicate carbon atom defects (D band) and in-plane vibrations of carbon atom sp^2 hybridization (G band), respectively (Fig. 2(a)) [24–26]. The I_D/I_G increases with the increase of material components and heterogeneous interfaces, indicating the increase of defects in the material. This may be due to the fact that more defects are introduced during the vulcanization process with the increase of components, while providing certain polarization active sites that contribute to the enhanced polarization relaxation. The samples were further analyzed by XPS. In the total XPS spectra, it was able to observe the presence of S, C, and V elements in all the samples, while the addition of W element in VS_2@C@WS_2 proved the successful introduction of WS_2 and the successful synthesis of the multicomponent material (Fig. 2(b)). In V 2p spectrum, the peaks at 523.6 and 516.0 eV correspond to V $2p_{1/2}$ and V $2p_{3/2}$ of V^{4+}, respectively. diffraction peaks at 521.4 and 513.8 eV at lower binding energies can be attributed to V^{2+} (Fig. 2(c)). the presence of V^{2+} results from the presence of unsaturated sulfur at the edges of the VS_2 crystal structure [27]. In S 2p spectrum, the diffraction peaks at 164.56, 162.7, and 169.0 eV in the single-phase VS_2 samples corresponded to S $2p_{1/2}$, S $2p_{3/2}$, and S–O [28]. The peak of S 2p is shifted to some extent by the introduction of other C or WS_2 components, which may be attributed to the introduction of heteroatoms leading to changes in the grain size of the material and the creation of defects (Fig. 2(d)). In C 1s spectrum, the diffraction peaks at 283.87, 284.47, and 285.25 eV correspond to C–C, C–O, and C=O (Fig. 2(e)) [29]. For the W 4f spectrum, there exist diffraction peaks of W $4f_{5/2}$ located at 3.9 and 37.9 eV, and diffraction peaks of W $4f_{7/2}$ at 31.9 and 35.7 eV, which are attributed to W^{4+} and W^{6+}, respectively (Fig. 2(f)) [30]. The above analysis indicates that transition metal sulfides with different components were successfully prepared.

The microscopic morphology and structure of the materials were analyzed using SEM and TEM. VS_2 has a hierarchical structure of nanosheets with multiple nanosheets stacked and smooth nanosheet surfaces, (Figs. 3(a1) and 3(a2)). After carbon coating, the VS_2 nanosheets became rough but still retained the hierarchical structure (Figs. 3(b1) and 3(b2)). After further modification, WS_2 nanosheets grew on the surface of VS_2@C and were tightly coated on the surface of VS_2@C material, forming VS_2@C@WS_2 composites with multi-phase heterogeneous structure (Figs. 3(c1) and 3(c2)). The lattice information of the materials was analyzed by HRTEM. In Fig. 3(a3), the lattice spacing of 0.28 nm corresponds to the (002) crystalline surface of VS_2, which is shown in its SAED diffraction image. After carbon coating, the (101) crystal plane of VS_2 can still be observed (Fig. 3(b3)). In Fig. 3(c3), the lattice spacing of 0.25 and 0.61 nm corresponds to the (011) crystalline surface of VS_2 and the (002) crystalline surface of WS_2, respectively, which further confirms the successful preparation of the multiphase heterostructured VS_2@C@WS_2 composites. The successful introduction of W, S, C, and V elements was shown in the EDS elemental mapping images (Fig. 3(d)).

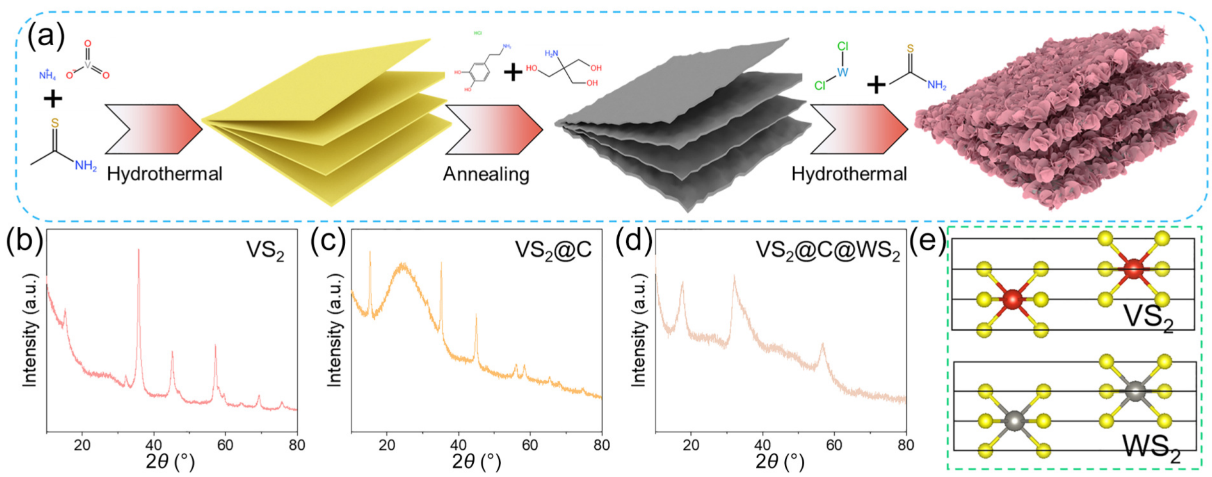

Figure 1 (a) Flowchart of sample preparation. XRD images of (b) VS_2, (c) VS_2@C, and (d) VS_2@C@WS_2. (e) Crystal structure images of VS_2 and WS_2.

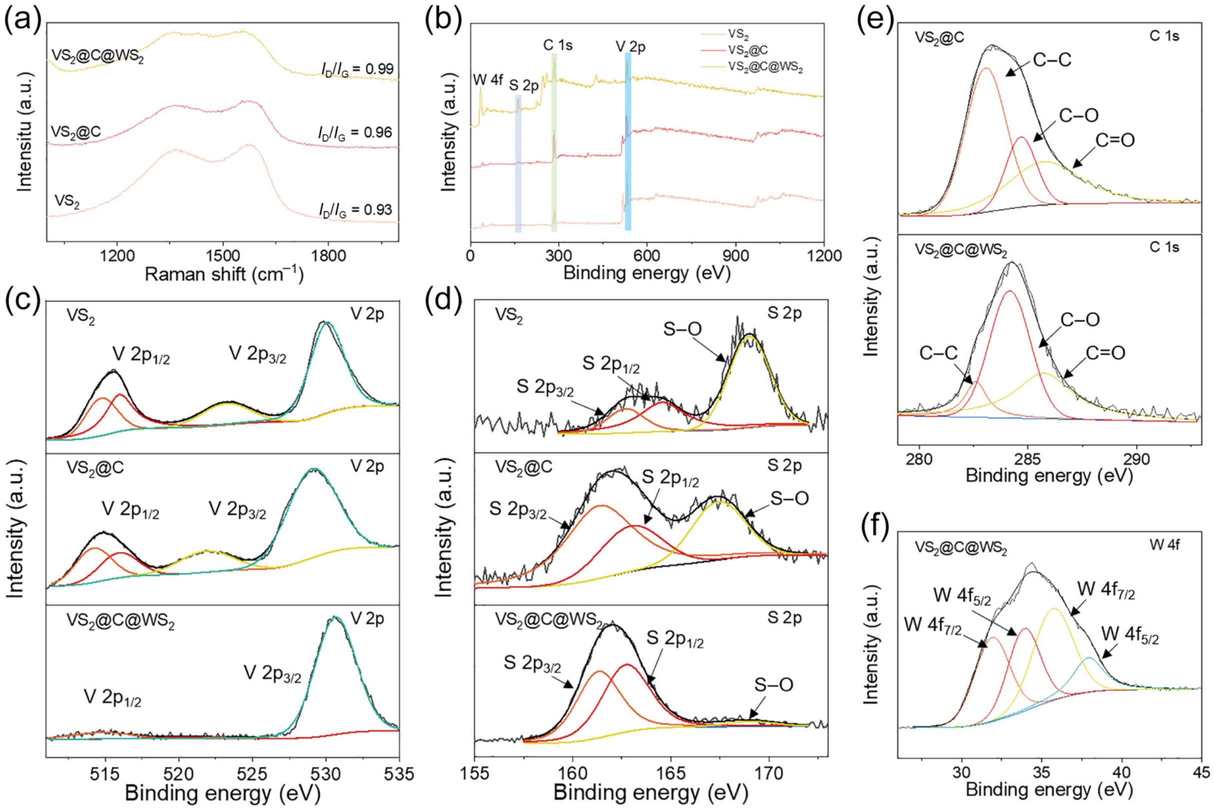

Figure 2 (a) Raman information. (b) XPS total, (c) V 2p, (d) S 2p, (e) C 1s, and (f) W 4d spectra for VS_2, VS_2@C, and VS_2@C@WS_2.

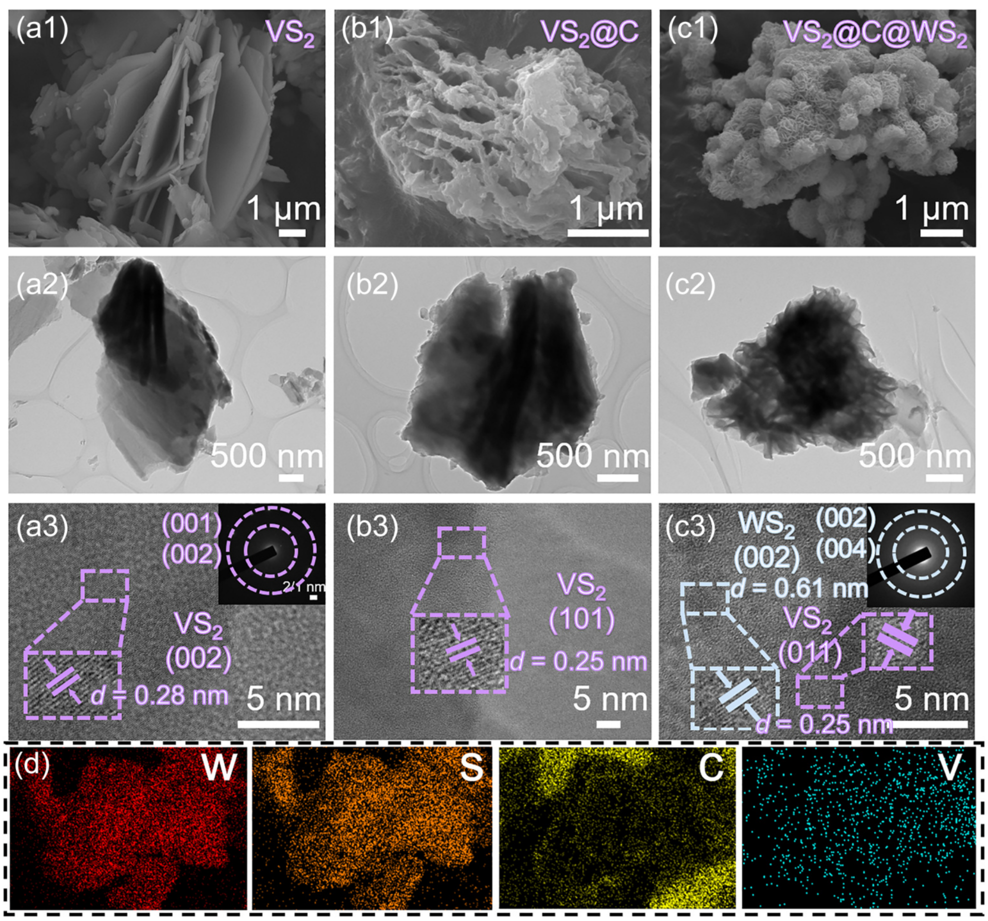

Figure 3 (a1)–(a3) SEM, (b1)–(b3) TEM, and (c1)–(c3) HRTEM images of VS_2, VS_2@C, and VS_2@C@WS_2. (d) EDS element mapping images of VS_2@C@WS_2.

Tsinghua University Press | SciOpen

The EMW absorption properties of the materials were evaluated by vector network analyzer tests [31, 32]. The minimum reflection loss (RL_{min}) and maximum effective absorption bandwidth (EAB_{max}) of the single-component VS_2 material were −37.3 dB and 6.3 GHz, respectively (Figs. 4(a1) and 4(a2)). Although VS_2 has a large EAB, its matched thickness of 6.3 mm is too thick and has poor absorption strength. After passing through the composite carbon component, the absorption strength and matching thickness were improved, exhibiting −41.4 dB and 5.04 GHz at 4.2 and 2.6 mm, respectively (Figs. 4(b1) and 4(b2)). This is due to the effect of heterogeneous interfaces between the two different materials, which improves the EMW absorption performance. By further compositing the WS_2 component with the VS_2@C component to obtain more heterogeneous interfaces, the EMW absorption performance was further improved, and a strong absorption of −66.35 dB and a broad EAB of 5.12 GHz were realized at 2.83 and 2.4 mm, respectively (Figs. 4(c1) and 4(c2)). This is mainly due to the strong interfacial polarization effect generated by the multiple heterogeneous interfaces formed by the three materials with different properties. As can be seen in Figs. 4(d) and 4(e), the VS_2@C@WS_2 composites with multicomponent and heterogeneous interfaces have strong absorption and broad bandwidth properties at thin matching thicknesses, further confirming their excellent EMW absorption properties. At thinner thicknesses, the EAB of the VS_2@C@WS_2 composites is mainly concentrated in the 8–16 GHz range and has a significant advantage in EMW absorption performance compared to VS_2 and VS_2@C (Fig. 4(f) and Fig. S1 in the ESM).

The EMW absorption capacity of the material is further analyzed by testing the electromagnetic parameters [33–35]. The dielectric loss capability of the materials was evaluated using the complex dielectric constant ($\varepsilon_r = \varepsilon' - j\varepsilon''$) [36]. The magnetic losses are negligible as the contribution of magnetic losses is not significant in this study (Fig. S2 in the ESM). In the dielectric parameter image, VS_2@C@WS_2 has the largest ε' and ε'' value, indicating a strong dielectric loss capability, and the fluctuation of the curve is attributed to the effect of polarization relaxation (Figs. 5(a) and 5(b)). The VS_2@C@WS_2 still maintains a large tan value in the dielectric loss tangent curve, which proves its good dielectric loss performance (Fig. 5(c)). By calculating the average values of samples ε' and ε'', VS_2@C@WS_2 has significantly stronger dielectric loss values compared to the one-component and two-component materials, which again proves its excellent dielectric loss performance (Figs. 5(d) and 5(e)). The dielectric loss capability of the material is further characterized by calculating the conductivity ($\sigma = \omega\varepsilon_0\varepsilon''$) of the material, which is enhanced as the material component increases, consistent with the dielectric loss of the material (Fig. S3 in the ESM) [37, 38]. This is mainly due to a combination of synergistic effects of multiphase materials and optimization of multiscale conduction mechanisms. Among them, C is used as an intermediate layer to connect VS_2 and WS_2 to form a three-dimensional (3D) conductive network, which can effectively reduce carrier scattering and enhance EMW absorption performance. The EMW attenuation capability was further evaluated using the attenuation constant (α), which is expressed by the following equation [39–41]

$$\alpha = \frac{\sqrt{2}\pi f}{c} \times \sqrt{(\mu''\varepsilon'' - \mu'\varepsilon') + \sqrt{(\mu''\varepsilon'' + \mu'\varepsilon')^2 + (\mu'\varepsilon'' - \mu''\varepsilon')^2}} \tag{3}$$

In Fig. 5(f), VS_2@C@WS_2 has the largest α value and exhibits the strongest EMW decay ability. According to the Debye theory, the polarization relaxation process of the material was analyzed by

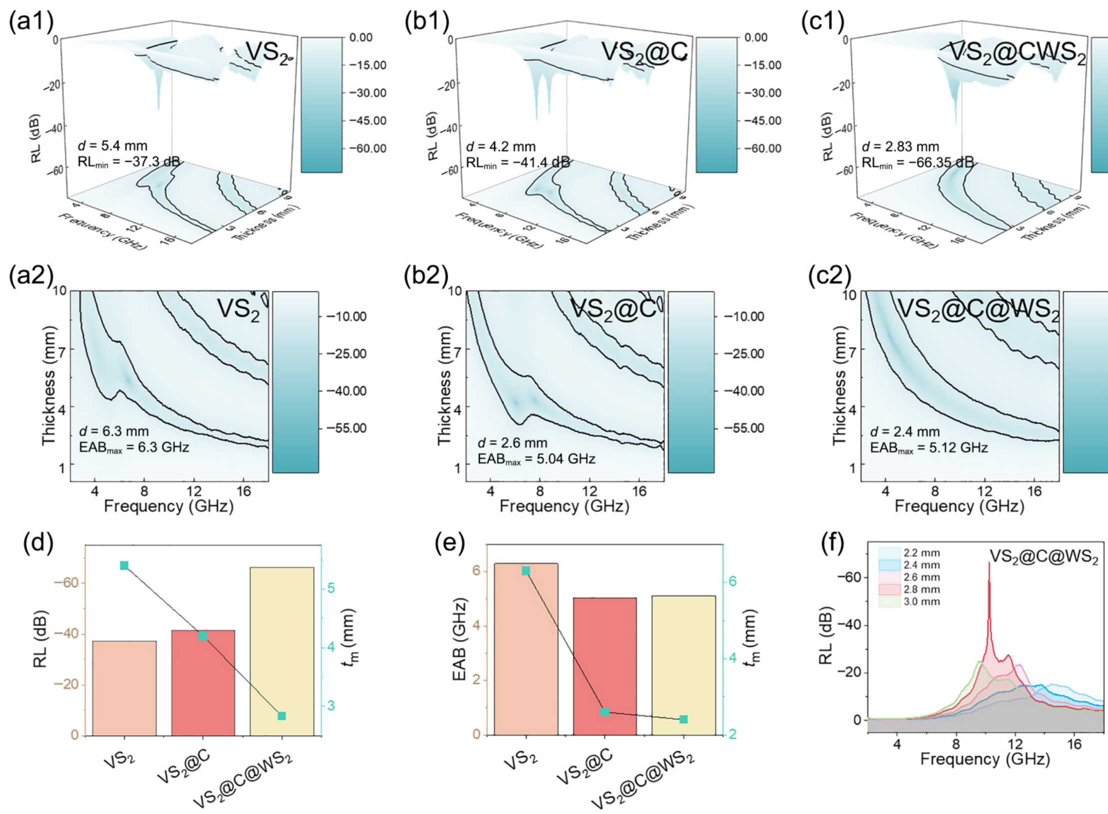

Figure 4 Information on the electromagnetic wave absorption properties of all samples.

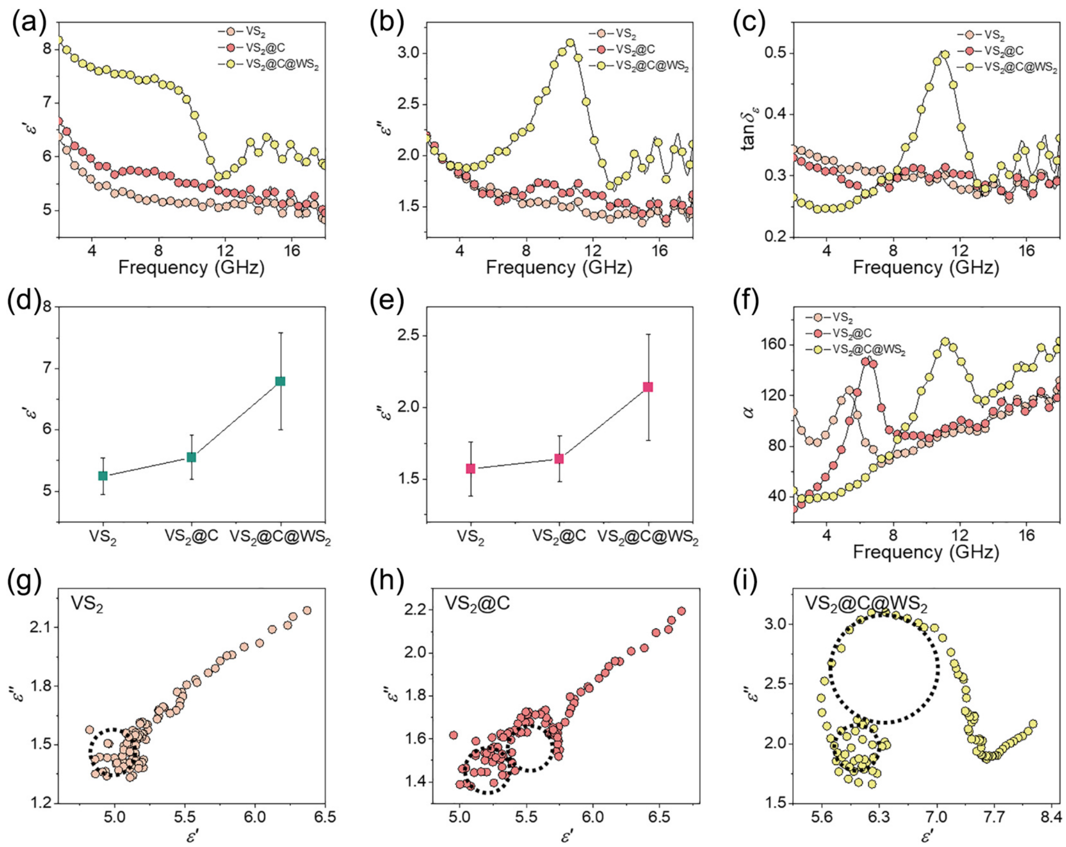

Figure 5 Complex permittivity for VS_2, VS_2@C, and VS_2@C@WS_2. (a) Real part, (b) imaginary part, (c) dielectric loss tangent, (d) dielectric real part mean, (e) dielectric imaginary part mean, (f) attenuation constant, and (g)–(i) Cole–Cole curves.

plotting Cole–Cole images, and the relevant equations are shown below [42, 43]

$$\left(\varepsilon' - \frac{\varepsilon_s + \varepsilon_\infty}{2}\right)^2 + (\varepsilon'')^2 = \left(\frac{\varepsilon_s - \varepsilon_\infty}{2}\right)^2 \quad (4)$$

All samples exhibit different polarization relaxation phenomena, with VS_2@C@WS_2 being the most significant (Figs. 5(g)–5(i)). Based on the relationship between ε' and ε''/f, the polarization relaxation time of the material was explored using Eq. (5) to further analyze the polarization relaxation process [44, 45].

$$\varepsilon' = \frac{1}{2\pi\tau}\frac{\varepsilon''}{f} + \varepsilon_\infty \quad (5)$$

In Fig. S4 in the ESM, materials with different compositions correspond to different polarization relaxation times, where VS_2@C@WS_2 has two polarization relaxation times. This can be attributed to the role of the heterogeneous interfaces formed between the multicomponent materials, which promotes the migration and hopping of charge carriers at the interfaces and enhances the polarization-depletion process. Impedance matching is an important parameter to characterize the EMW absorption performance of materials. The impedance matching properties were evaluated by calculating the area of $|Z_{in}/Z_0|$ in the range of 0.8–1.2 [46, 47]. The single-component VS_2 material showed poor impedance matching performance, and the multicomponent VS_2@C and VS_2@C@WS_2 exhibited better impedance matching performance, which provided excellent EMW absorption performance (Figs. S5 and S6 in the ESM).

The radar cross section (RCS) simulation of the materials was performed using CST to evaluate the radar stealth capability of the materials [48–50]. Compared with pure perfect electric conductor (PEC), all component materials exhibit some RCS attenuation capability. Particularly noteworthy is that VS_2@C@WS_2 with a multiphase heterogeneous interface has the strongest attenuation ability, which is consistent with the EMW absorption properties (Figs. 6(a1)–6(a4)). By analyzing the RCS attenuation values at different angles, the attenuation ability is different at different angles (Figs. 6(b1)–6(b3) and Fig. S7 in the ESM). The RCS attenuation values at 0°, 15°, 30°, 45°, 60°, 75°, and 90° were calculated, and it was found that VS_2@C@WS_2 had the strongest attenuation ability at 0° (Fig. 6(c)). The two-dimensional lamellar structure of VS_2 and WS_2 has a large specific surface area, which effectively enhances the multiple scattering of EMW [51–53]. The presence of heteroatoms and the S vacancies introduced during the vulcanization process form defective polarization sites, which produce dipole polarization effects when an applied magnetic field is applied. The contact of different materials formed heterogeneous interfaces, leading to the aggregation of charge carriers at the interfaces and the interfacial polarization effect, which was further enhanced by the action of multiple heterogeneous interfaces (Fig. 6(d)) [54–56]. In summary, the prepared VS_2@C@WS_2 composites with a multiphase structure achieve excellent EMW absorption properties through the synergistic effect of multiple mechanisms.

4 Conclusions

In this study, multi-component transition metal sulfide composites

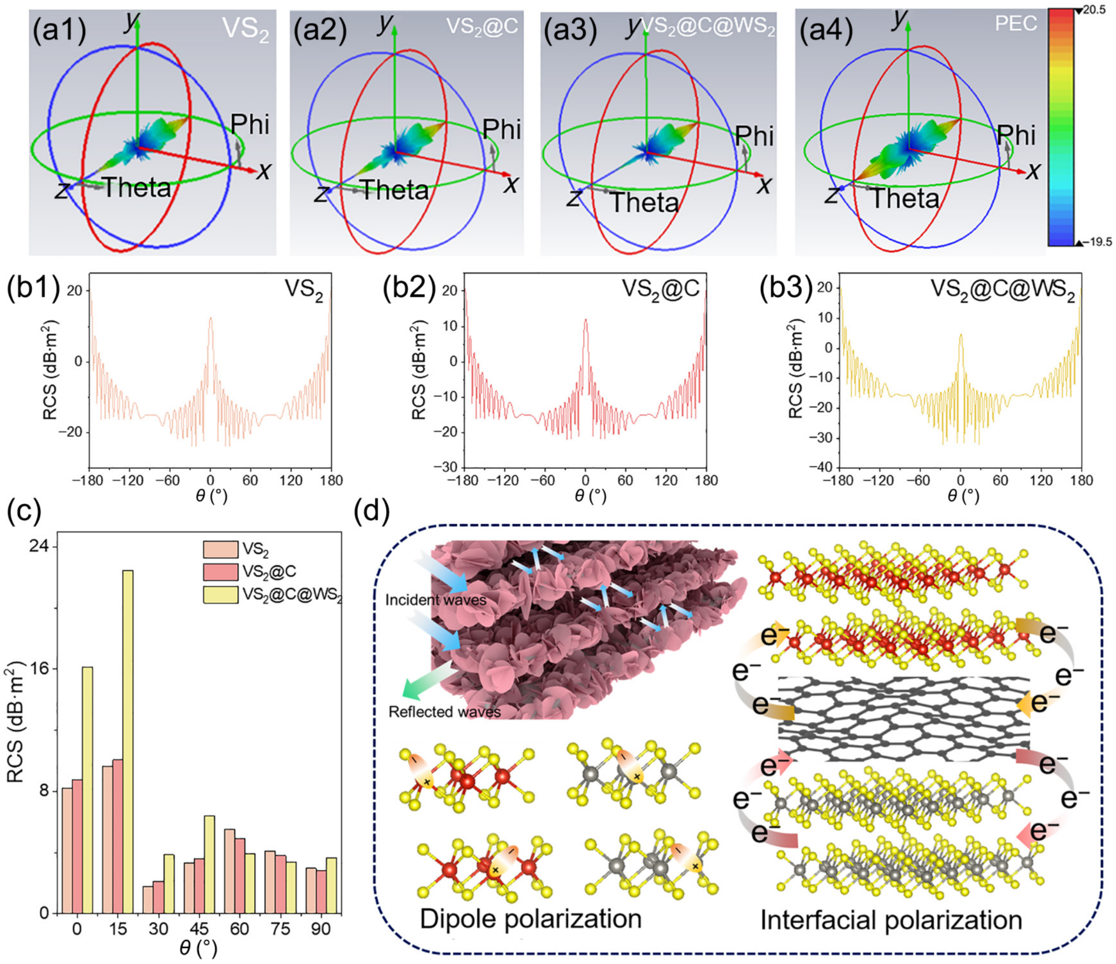

Figure 6 (a1)–(a4) 3D and (b1)–(b3) 2D RCS attenuation images; (c) RCS attenuation values at different angles of VS_2, VS_2@C, and VS_2@C@WS_2. (d) Absorption mechanism diagram for VS_2@C@WS_2.

were prepared by a simple process, such as hydrothermal synthesis and high-temperature carbonization, to construct multiple heterogeneous interfaces. The heterogeneous interface structures of the composites were precisely controlled by adjusting the components of the materials, thus improving the polarization loss capability. At the heterogeneous interfaces formed between different components, space charge regions were established, which effectively promoted the interfacial polarization loss. Finally, VS_2@C@WS_2 with abundant heterogeneous interfaces obtained ideal EMW absorption properties, realizing an absorption intensity of −66.35 dB and absorption band of 5.12 GHz. This work provides valuable insights into compositionally modulated inhomogeneous interfaces and broadens the avenues for the application of multiphase structural composites in EMW absorption.

Electronic Supplementary Material: Supplementary material (RL images of samples at different thicknesses, magnetic permeability parameters, conductivity, Cole–Cole plots, impedance matching area, impedance matching at different thicknesses, and 2D polar coordinate images) is available in the online version of this article at https://doi.org/10.26599/NR.2025.94907808.

Data availability

All data needed to support the conclusions in the paper are presented in the manuscript. Additional data related to this paper may be requested from the corresponding author upon request.

Acknowledgements

This work is financially supported by the National Natural Science Foundation of China (Nos. 52377026 and 52301192), Taishan Scholars and Young Experts Program of Shandong Province (No. tsqn202103057), Natural Science Foundation of Shandong Province (Nos. ZR2024ME046 and ZR2024QE313), and Postdoctoral Science Foundation of China (No. 2024M761554).

Declaration of competing interest

All the contributing authors report no conflict of interests in this work.

Author contribution statement

Z. Q. G.: Writing manuscript. Y. H. C: Writing manuscript. D. L.: Project administration, writing manuscript. S. Y. Z.: Data curation. Z. R. J.: Project administration, funding acquisition, writing manuscript. G. L. W.: Project administration, writing manuscript.

Use of AI statement

None.

References

[1] Huang, M. Q.; Wang, L.; Pei, K.; Li, B. X.; You, W. B.; Yang, L. T.; Zhou, G.; Zhang, J. C.; Liang, C. Y.; Che, R. C. Heterogeneous interface engineering of Bi-metal MOFs-derived $ZnFe_2O_4$-ZnO-Fe@C microspheres via confined growth strategy toward superior electromagnetic wave absorption. *Adv. Funct. Mater.* **2024**, *34*, 2308898.

[2] Sheng, D. H.; Song, Z. R.; Cheng, S. Y.; Wang, W. Q.; Chen, Z. L.; Gao, R. R.; Li, W. J.; Xie, A. M. Defect-rich carbon nanosheets derived from $p(C_3O_2)_x$ for electromagnetic wave absorption applications. *Carbon* **2024**, *230*, 119637.

[3] Gu, Y. H.; Chen, Z. Y.; Wang, Z. C.; Yu, S. F.; Bi, L. Avoiding undesirable cathode/electrolyte interfacial reactions for proton-conducting solid oxide fuel cells by Joule heating. *J. Adv. Ceram.* **2025**, *14*, 9221040.

[4] Chen, Z. L.; Zhang, J. H.; Ni, L. Y.; Sheng, D. H.; Gao, R. R.; Li, W. J.; Xie, A. M. Improving electromagnetic wave absorption property of metal borides/carbon nanocomposites by magnetic-electric balance and ion substitution tuning strategy. *Carbon* **2024**, *221*, 118901.

[5] Cheng, S. Y.; Sheng, D. H.; Mukherjee, S.; Dong, W.; Huang, Y. B.; Cao, R.; Xie, A. M.; Fischer, R. A.; Li, W. J. Carbon nanolayer-mounted single metal sites enable dipole polarization loss under electromagnetic field. *Nat. Commun.* **2024**, *15*, 9077.

[6] Yele, M.; Sarula, G.; Yang, J.; Yang, L.; Zhang, H.; Chen, L. F.; Zhang, X. M.; Wang, J. H.; Wang, T. Y.; Jin, C. Z. et al. Integrated structural-functional MXene-GNs/ANF flexible composite film with enhanced thermal conductivity and electromagnetic interference shielding performance. *J. Mater. Sci. Technol.* **2026**, *241*, 200–210.

[7] Zhong, X.; He, M. K.; Zhang, C. Y.; Guo, Y. Q.; Hu, J. W.; Gu, J. W. Heterostructured BN@Co-C@C endowing polyester composites excellent thermal conductivity and microwave absorption at C band. *Adv. Funct. Mater.* **2024**, *34*, 2313544.

[8] Shen, Y.; Ma, Z. Q.; Yan, F.; Zhu, C. L.; Zhang, X. T.; Chen, Y. J. Enhanced interfacial polarization loss of FeS/MoS_2@N-doped carbon sandwich-walled nanotubes enables high-performance electromagnetic wave absorption. *Adv. Funct. Mater.* **2025**, *35*, 2423947.

[9] Liu, J. L.; Yin, M. X.; Liu, Z. L.; Ren, J. K.; Bian, H.; Zhou, X. J.; Lv, X. Y.; Qu, D.; Tao, K.; Wei, B. et al. Solvent-engineered *in-situ* heterogenization of copper-based sulfides for broadening electromagnetic wave absorption. *Chem. Eng. J.* **2025**, *507*, 160742.

[10] Han, Y. X.; Guo, H.; Qiu, H.; Hu, J. W.; He, M. K.; Shi, X. T.; Zhang, Y. L.; Kong, J.; Gu, J. W. Multimechanism decoupling for low-frequency microwave absorption hierarchical Fe-doped Co magnetic microchains. *Adv. Funct. Mater.*, in press, DOI: 10.1002/adfm.202506803.

[11] Shi, M. J.; Jia, Z. R.; Lan, D.; Gao, Z. G.; Zhang, S. Y.; Wu, G. L. Enhanced polarization relaxation of multidimensional bimetallic selenide nanocomposites for electromagnetic wave absorption. *Adv. Funct. Mater.*, in press, DOI: 10.1002/adfm.202502261.

[12] Cheng, S. Y.; Zhou, Q. L.; Sheng, D. H.; Dong, W.; Dou, J. H.; Huang, Y. B.; Cao, R.; Xie, A. M.; Fischer, R. A.; Mukherjee, S. et al. Cu-X bonds regulated conduction and polarization loss in conductive metal-organic framework under electromagnetic field. *Adv. Sci.*, in press, DOI: 10.1002/advs.202508379.

[13] Li, Y.; Dong, C. L.; Wang, S. J.; Lei, D. Y.; Yin, B. B.; Cui, Y. F.; Wang, Y. R.; Li, R. Micro-macro regulating heterogeneous interface engineering in 3D N-doped carbon fiber/MXene/TiO_2 Nano-aerogel for boosting electromagnetic wave absorption. *Nano Res.* **2025**, *18*, 94907169.

[14] Wang, J. E.; Song, T. L.; Ming, W.; Yele, M.; Chen, L. F.; Zhang, H.; Zhang, X. J.; Liang, B. L.; Wang, G. S. High MXene loading, nacre-inspired MXene/ANF electromagnetic interference shielding composite films with ultralong strain-to-failure and excellent Joule heating performance. *Nano Res.* **2024**, *17*, 2061–2069.

[15] Li, C. L.; Piao, M. X.; Zhang, H.; Wang, X. Constructing of Co nanosheets decorating with WS_2 nanoclusters for enhanced electromagnetic wave absorption. *J. Alloy. Compd.* **2022**, *912*, 165269.

[16] Wang, H. H.; Zhang, H. B.; Cheng, J. Y.; Liu, T. T.; Zhang, D. Q.; Zheng, G. P.; Zhai, S. R.; Cao, M. S. Building the conformal protection of VB-group VS_2 laminated heterostructure based on biomass-derived carbon for excellent broadband electromagnetic waves absorption. *J. Materiomics* **2023**, *9*, 492–501.

[17] Lei, D. Y.; Yu, L.; Wang, S. J.; Li, Y.; Jia, H. X.; Wu, Z. Y.; Bao, J. W.; Liu, J. P.; Xi, X.; Su, L. A state-of-the-art on electromagnetic and mechanical properties of electromagnetic waves absorbing cementitious composites. *Cem. Concr. Compos.* **2025**, *157*, 105889.

[18] Zhou, L.; Hu, P. F.; Bai, M.; Leng, N.; Cai, B.; Peng, H. L.; Zhao, P. Y.; Guo, Y. Q.; He, M. K.; Wang, G. S. et al. Harnessing the electronic spin states of single atoms for precise electromagnetic modulation. *Adv. Mater.* **2025**, *37*, 2418321.

[19] Zhang, S. J.; Zheng, J. J.; Zhao, Z. W.; Du, S. X.; Lan, D.; Gao, Z. G.; Wu, G. L. New prospects in built-in electric fields for electromagnetic wave absorption: From fundamentals to interdisciplinary applications. *Adv. Funct. Mater.*, in press, DOI: 10.1002/adfm.202513762.

[20] Gu, W. H.; Luo, Z. T.; Wang, J.; Tan, X.; Tao, Z.; Zhou, P. P.; Zhang, H. Y.; Lan, D.; Xia, A. L. Multifunctional lightweight rGO/polyimide hybrid aerogels for highly efficient infrared-radar-acoustic compatibility via heterogeneous interface engineering strategies. *J. Mater. Sci. Technol.* **2026**, *243*, 102–114.

[21] Li, Y.; Lu, Y. H.; Liu, Z. X.; Lei, D. Y.; Yang, M. L.; Yang, D. L.; Jin, Y. H.; Liu, J. X.; Lan, D. Construction of cotton derived carbon fiber@FeNi nanoparticle/porous carbon sponge for boosting electromagnetic wave absorption. *Rare Metals* **2025**, *44*, 6531–6546.

[22] Pan, Y. L.; Cheng, L.; Lan, D.; Zhang, S. Y.; He, M. K.; Wu, G. R.; Gao, Z. G.; Jia, Z. R.; Wu, G. L. Conductor-semiconductor heterointerface polarization enhancement for superior electromagnetic wave absorption. *J. Mater. Sci. Technol.* **2026**, *244*, 129–141.

[23] Liu, X. D.; Zhang, S.; Yu, M.; Zhao, X. X.; Jia, Y. W.; Huang, Y.; Zong, M. WS_2 nanosheets anchored on N-doped carbon fibers for superior electromagnetic wave absorption. *Chem. Eng. J.* **2023**, *465*, 142932.

[24] Zhang, Y.; Zhang, S. Y.; Lan, D.; Yao, J. H.; Gao, Z. G.; Wu, G. L.; Jiao, J. Multiple charge carriers manipulation toward semiconductive ceramic nanocomposites for corrosion-resistant electromagnetic wave absorption. *Small* **2025**, *21*, 2500581.

[25] He, M. K.; Zhong, X.; Lu, X. H.; Hu, J. W.; Ruan, K. P.; Guo, H.; Zhang, Y. L.; Guo, Y. Q.; Gu, J. W. Excellent low-frequency microwave absorption and high thermal conductivity in polydimethylsiloxane composites endowed by hydrangea-like CoNi@BN heterostructure fillers. *Adv. Mater.* **2024**, *36*, 2410186.

[26] Tang, L.; Jiang, J.; He, M. K.; Zhang, Y. L.; Hu, Q. Y.; Liu, X. L.; Liu, X.; Qiu, H. Lightweight PBO nanofiber@ZIF-67 derived carbon aerogel with superior electromagnetic wave absorption and thermal insulation. *J. Mater. Sci. Technol.* **2026**, *244*, 186–195.

[27] Li, E. Z.; Wang, M. S.; Hu, X.; Huang, S. M.; Yang, Z. L.; Chen, J. C.; Yu, B.; Guo, B. S.; Ma, Z. Y.; Huang, Y. et al. NH_4^+ pre-intercalation and Mo doping VS_2 to regulate nanostructure and electronic properties for high efficiency sodium storage. *Small* **2024**, *20*, 2308630.

[28] Hou, X.; Feng, X. R.; Jiang, K.; Zheng, Y. C.; Liu, J. T.; Wang, M. Recent progress in smart electromagnetic interference shielding materials. *J. Mater. Sci. Technol.* **2024**, *186*, 256–271.

[29] Liu, T. T.; Wang, Y. C.; Wang, Y. Z.; Cao, M. S. "Heterodimensional structure" integrated defect and interface engineering for efficiently EMI shielding and electrochemical response. *Adv. Funct. Mater.* **2025**, *35*, 2404280.

[30] Xu, J.; Shu, R. W.; Wan, Z. L.; Shi, J. J. Construction of three-dimensional hierarchical porous nitrogen-doped reduced graphene

oxide/hollow cobalt ferrite composite aerogels toward highly efficient electromagnetic wave absorption. *J. Mater. Sci. Technol.* **2023**, *132*, 193–200.

[31] Zhao, J.; He, M. K.; Guo, H.; Zhang, Y. L.; Qiu, H.; Lai, H. R. Multidimensional construction of 1T-MoS_2@graphene nanosheets nanocomposites for enhanced electromagnetic wave absorption. *J. Mater. Sci. Technol.* **2025**, *218*, 35–44.

[32] Wu, Z. M.; Huang, J.; Zeng, X. J. Dual magnetic particles modified carbon nanosheets in CoFe/Co@NC heterostructure for efficient electromagnetic synergy. *Soft Sci.* **2024**, *4*, 42.

[33] Yu, B. W.; Jia, Z. R.; Lv, C. P.; Ma, G. S.; Liu, X. H.; Lan, D.; Zhang, S. Y.; Gao, Z. G.; Zhu, Z. J.; Wu, G. L. Antimony-hybridization engineering in p-n heterojunctions for optimized electromagnetic wave absorption. *Small* **2025**, *21*, 2500918.

[34] Li, Y. K.; Zhai, W. H.; Wang, G. Z.; Deng, Y.; Du, S. M.; Li, S. R.; Fu, C. Y.; Lan, D.; Zhang, S. Y.; Wang, X. X. et al. Photoacoustic synchronization system based on anisotropic nanofibers. *Nano Res.* **2025**, *18*, 94907470.

[35] Wang, X. Y.; Liu, J.; Han, X. K.; Deng, A.; Han, B. W.; Jin, Y. H.; Lan, D.; Ma, M. L.; Li, Y. One-dimensional multicomponent nanofibers engineered as heterostructures for electromagnetic stealth applications. *J. Alloy. Compd.* **2025**, *1028*, 180631.

[36] Xiong, S. X.; Cai, L. J.; Zhang, Y.; Ma, Y.; Lan, D.; Chen, G.; Dong, C. J.; Guan, H. T. Catalytically tuned $Bi_2Fe_4O_9$-polypyrrole heterostructures: Multifunctional electromagnetic wave absorbers with enhanced stealth and thermal camouflage. *Rare Met.* **2025**, DOI: 10.1007/s12598-025-03439-z.

[37] Zhou, J. X.; Lan, D.; Zhang, F.; Cheng, Y. H.; Jia, Z. R.; Wu, G. L.; Yin, P. F. Self-assembled MoS_2 cladding for corrosion resistant and frequency-modulated electromagnetic wave absorption materials from X-band to Ku-band. *Small* **2023**, *19*, 2304932.

[38] Zhang, Y.; Lan, D.; Hou, T. Q.; Jia, M. S.; Jia, Z. R.; Gu, J. W.; Wu, G. L. Multifunctional electromagnetic wave absorbing carbon fiber/$Ti_3C_2T_X$ MXene fabric with ultra-wide absorption band. *Carbon* **2024**, *230*, 119594.

[39] Fan, X. X.; Zhang, X. C.; Li, L.; Cao, M. S. Recent progress and perspective of microwave absorption materials derived from metal-organic frameworks. *Soft Sci.* **2024**, *4*, 43.

[40] Li, Y.; Liu, Z. X.; Lu, Y. H.; Yang, M. L.; Zhang, P.; Lei, D. Y.; Liu, C. K.; Wang, S. J.; Dong, C. L. Surface energy induced microstructural engineering of bio-derived N-doped carbon fibers anchored by CoNi nanoparticles for superior microwave absorption. *Adv. Compos. Hybrid Mater.* **2025**, *8*, 176.

[41] Dong, X. C.; Yu, S. F.; Gu, Y. Y.; Bi, L. Tailoring $SrFeO_3$ cathode with Ta and F allows high performance for proton-conducting solid oxide fuel cells. *Sustain. Mater. Techno.* **2024**, *41*, e01104.

[42] Zhu, J. H.; Cheng, L.; Zhang, S. Y.; Lan, D.; Wu, G. R.; Gao, Z. G.; Jia, Z. R. 0D/1D hollow heterogeneous structure to induce self-assembly of CNTs for optimized self-anticorrosion and electromagnetic wave absorption performance. *Carbon* **2025**, *238*, 120310.

[43] Cao, R. B.; Qiu, Y.; Zhao, X. N.; Lan, D.; Lu, Y. M.; Wang, Z. Q.; Xu, H. Y.; Liu, Y. C. Carbon-$CoFe_2O_4$ composite with hierarchical porous structure for efficient microwave absorption. *Diam. Relat. Mater.* **2025**, *157*, 112542.

[44] Yin, Y. R.; Huang, H. F.; Boulfrad, S.; Dai, H. L.; Gu, Y. Y.; Yu, S. F.; Bi, L. Breaking the limits of Ruddlesden-Popper cathodes to achieve a game-changer for proton-conducting solid oxide fuel cells. *Energy Environ. Sci.*, in press, DOI: 10.1039/D5EE00993F.

[45] Liu, J. K.; Pan, Y. L.; Yu, L. Y.; Gao, Z. G.; Zhang, S. Y.; Lan, D.; Jia, Z. R.; Wu, G. L. MoS_2-based composites for microwave absorption mechanism-oriented structural optimization and design perspectives. *Carbon* **2025**, *238*, 120233.

[46] Zhang, S.; Li, M. R.; Chen, G. N.; Wang, H. L.; Shao, G.; Lan, D.; Zhu, Y. Q.; Zhang, R.; Guan, L.; Fan, B. B. Achieving high performance microwave attenuation by anchoring magnetic CoNi nanoparticles onto few-layer $Ti_3C_2T_x$ MXene. *J. Alloy. Compd.* **2025**, *1023*, 180015.

[47] Yin, X.; Yang, Q. J.; Xia, S. H.; Zhai, J. F.; Wang, Y. D.; Song, L. X.; Wu, Z. Y.; Xiong, J.; Wong, W. Y. Advanced interface design of direct-current tribovoltaic nanogenerator. *Adv. Mater.* **2025**, *37*, 2417254.

[48] Liu, X. X.; Chen, J. T.; Lan, D.; Hu, J. H.; Zhang, S. Y.; Lv, Q. Y.; Xiu, L. H.; Yu, W. Z.; Liu, D.; Wu, G. L. Synergistic polarization effect of selenium-deficient quantum dots integrated carbon nanotubes for superior electromagnetic wave absorption. *Compos. Commun.* **2025**, *56*, 102390.

[49] Guo, Z. Q.; Ren, J. W.; Xu, X. Z.; Lan, D.; Zhang, S. Y.; He, M. K.; Gao, Z. G.; Jia, Z. R.; Wu, G. L. Multiphase Co/Ni metal nitrides with heterointerfaces for enhanced interfacial polarization loss in electromagnetic wave absorption. *J. Mater. Sci. Technol.* **2025**, *236*, 19–27.

[50] Dai, H. L.; Boulfrad, S.; Chu, X. R.; Gu, Y. Y.; Bi, L.; Zhang, Q. F. $La_{0.5-x}Sc_xSr_{0.5}MnO_{3-\delta}$ cathodes for proton-conducting solid oxide fuel cells: Taking advantage of the secondary phase. *J. Adv. Ceram.* **2024**, *13*, 1759–1770.

[51] Wang, Z. X.; Jia, Z. R.; Ren, J. W.; Wang, L.; Lan, D.; Zhang, S. Y.; Shi, X. T.; Liu, X. H.; Gao, Z. G.; Wu, G. L. Multi-topological network engineering of Co/MnO composites for electromagnetic wave absorption. *J. Mater. Sci. Technol.* **2025**, *235*, 81–90.

[52] Shi, Y. T.; Xu, G. T.; Liang, G. Z.; Lan, D.; Zhang, S. Y.; Wang, Y. R.; Li, D. H.; Wu, G. L. PEG-VN modified PP separator for high-stability and high-efficiency lithium-sulfur batteries. *Acta Phys. Chim. Sin.* **2025**, *41*, 100082.

[53] Fang, G.; Liu, C. Y.; Wei, X. Y.; Cai, Q. Y.; Chen, C.; Xu, G. Y.; Ji, G. B. Determining the preferable polarization loss for magnetoelectric microwave absorbers by strategy of controllably regulating defects. *Chem. Eng. J.* **2023**, *463*, 142440.

[54] Fang, M.; Huang, L. Y.; Cui, Z. R.; Yi, P.; Zou, H. H.; Li, X. F.; Deng, G.; Chen, C. Y.; Geng, Z.; He, J. Z. et al. Phase-transition microcapacitor network in organohydrogel for absorption-dominated electromagnetic interference shielding and multi-mode intelligent responsiveness. *Adv. Funct. Mater.* **2025**, *35*, 2418870.

[55] Cheng, Y. H.; Liu, X.; Ren, J. W.; Xu, X. Z.; Lan, D.; Wu, G. R.; Zhang, S. Y.; Gao, Z. G.; Jia, Z. R.; Wu, G. L. Component-based modulation engineering to improve magnetoelectric coupling for self-anticorrosion broadband absorption. *Carbon* **2025**, *239*, 120325.

[56] Zhang, Y. H.; Zhang, L.; Si, H. X.; Zhang, Y.; Li, C. P.; Zhang, L.; Zhang, J. W.; Gong, C. H. TiN nanofiber metacomposites for efficient electromagnetic wave absorption: Insights on multiple reflections and scattering effects. *J. Mater. Sci. Technol.* **2025**, *233*, 69–79.